

# Influence of solid–fluid interaction on impact dynamics against rigid barrier: CFD–DEM modelling

JUN FANG\*, LIZHONG WANG\*, YI HONG† and JIDONG ZHAO‡

Both the solid and fluid phases in a debris flow vitally influence the impact dynamics against a rigid barrier. However, previous numerical and analytical models commonly adopt an equivalent fluid approach, which does not explicitly consider solid–fluid interaction when impacting a barrier. This study investigates the role of solid–fluid interaction on the impact mechanism and load exerted on a rigid barrier. A coupled computational fluid dynamics and discrete-element method (CFD–DEM) is used to study the effect of solid–fluid interaction on impact by varying the solid fraction from 0 to 0.5. The mesoscopic insight from CFD–DEM modelling reveals that the particle–fluid interaction plays two roles in increasing the kinematic energy of particles: (a) imposing driving force to the particles; (b) reducing inter-particle contact forces and therefore energy dissipation from shearing among grains by applying buoyancy to the particles. Consequently, the run-up height and impact pressure of the water–particle mixture flows at the barrier are higher than those of dry granular flows with the same Froude number ( $Fr$ ). While impacting the rigid barrier, most of the energy of water–particle mixtures (exhibiting a run-up mechanism) is dissipated as the fluid phase segregates from the mixture and rolls back towards subsequent flow. This differs from the conventional impact mechanism observed for dry granular flows, where the energy is mainly dissipated by way of shearing between layers of sand piling up behind a barrier.

KEYWORDS: discrete-element modelling; landslides; numerical modelling

## INTRODUCTION

The flow dynamics of debris flows are complicated by the interaction between the solid and the fluid phases. Solid–fluid interaction can alter pore fluid pressure, which in turn regulates the Coulomb friction within and at the boundary of a landslide (Iverson & George, 2014). The degree of interaction between the solid and fluid phases in the flow may be represented by volumetric solid fraction, which is defined as the ratio of the solid volume to the global volume of the packing (Iverson, 1997). Despite extensive investigations into the influence of solid–fluid interaction on the mobility of geophysical flows (Iverson, 1997; McArdell *et al.*, 2007; Iverson & George, 2014), less focus has been placed on the effect of flow composition on the impact behaviour of geophysical flows, such as granular flows, debris floods and debris flows. Choi *et al.* (2015a, 2015b) recognised the importance of the solid fraction and carried out pioneer experiments to investigate the solid–fluid interaction when impacting barriers. They reported that flows with a higher solid fraction more readily dissipate flow energy by way of shearing among grains. The flow composition dictates solid–fluid interaction, and therefore, significantly influences the mechanism of impact (Choi *et al.*, 2015a), which in turn governs the load distribution (Song *et al.*, 2017). Furthermore, Wendeler *et al.* (2006) and He *et al.* (2018) studied the impact behaviour of geophysical debris flows predominantly focused on the dynamic responses of the

structures. To bridge the knowledge gap, Ng *et al.* (2016) developed the world's first impact set-up along with a novel flexible barrier to model the impact dynamics of debris flow in the centrifuge. This unique model enables field stress conditions to be simulated. Using this model, Ng *et al.* (2017a) and Song *et al.* (2017) carried out a unique series of tests to model the impact behaviour of geophysical flows, on rigid and flexible barriers. Depending on the flow composition, Ng *et al.* (2017a) discovered that the impact behaviour differed significantly. For dry granular flows, the dissipation of the flow kinetic energy was significantly enhanced by way of stress-dependent friction, unlike viscous flows, which dissipated the flow kinetic energy less readily. Song *et al.* (2017) further studied a wider range of geophysical flows by using a centrifuge and was the first to demonstrate that an increase in solid fraction can lead to higher static impact load. They discovered that the increase in impact load was directly related to the formation of dead zones at the base of the barrier, which contributed static loading on top of dynamic loading simultaneously.

Numerical investigations of the interaction between structures and geophysical flows commonly apply continuum models (Chiou *et al.*, 2005; Peng *et al.*, 2016), discrete-element models (Teufelsbauer *et al.*, 2011; Utili *et al.*, 2015), computational fluid dynamics (CFD; Zakeri *et al.*, 2009) or coupled three-dimensional (3D) large-deformation finite elements (Hallquist, 2006; Kwan *et al.*, 2015). Koo *et al.* (2016) were pioneers in adopting a coupled 3D large-deformation finite-element model to simulate rock fall impacting a flexible barrier. The aforementioned methods have had limited success in providing insight on the mechanisms involved in the impact of debris flow against structural countermeasures. The limitations arise in modelling the interstitial fluid and its interaction with both the solid and fluid phases. The complicated debris mass is generally simplified by treating it as an equivalent fluid. However, it is evident that both the solid and fluid phases

Manuscript received 7 June 2019; revised manuscript accepted 13 January 2021.

\* Zhejiang University, Hangzhou, P. R. China.

† Zhejiang University, Hangzhou, P. R. China (corresponding author).

‡ Hong Kong University of Science and Technology, Kowloon, Hong Kong, P. R. China.

vitality influence debris flow dynamics (Iverson, 1997) and the gross simplifications using an equivalent fluid approach limit a comprehensive understanding of two-phase interaction. Recent advances in numerical modelling have applied the discrete-element method (DEM) to represent the solid phase, coupled with either CFD or the lattice Boltzmann method (LBM) representing the fluid phase (Zhao & Shan, 2013; Shan & Zhao, 2014; Kawano *et al.*, 2017; Su *et al.*, 2018). However, such two-phase computational techniques have yet to be explicitly calibrated using experimental results to examine debris flow impact problems. A well calibrated and coupled CFD–DEM model would undoubtedly offer new insights into the soil–fluid interaction, stress and energy dissipation within the debris mass, and thus the impact dynamics of the debris flow against structural countermeasures. An improved understanding in turn provides opportunities for optimising the design of debris-resisting barriers (Kwan, 2012) and more importantly for dual-barrier systems, which are found to be more environmentally friendly and are well suited to congested cities (Ng *et al.*, 2018).

In this study, a series of flume tests was simulated using a coupled CFD–DEM method to investigate the effects of particle–fluid interaction on the mobility of a debris flow, and on its impact dynamics against a rigid barrier. The degree of particle–fluid interaction is represented by the volumetric solid fraction,  $v_s$ . Relatively dry granular flows are adopted as control tests. The calibrated and coupled CFD–DEM model not only reveals the fundamental impact mechanisms for two-phase flows, but provides a quantitative understanding of the mesoscopic fluid–particle interactions.

## METHODOLOGY AND MODEL VALIDATION

### Methodology

Debris flow is considered to consist of particles and fluids, ignoring the gas phase that is usually present in nature (Hong *et al.*, 2020). The solid particles are regarded as a discrete phase, which is modelled by the DEM, while the fluid is a continuous system and is simulated by the CFD method. In this study, the solid particles and their interactions are modelled by the DEM, while the fluid is a continuous system being simulated by the CFD method. The motion of particles in DEM is governed by Newton's equation, and the fluid in CFD is controlled by the Navier–Stokes equation. The solid and the fluid phase are then coupled by considering the drag force and buoyant force acting on the particles by the fluid through CFD–DEM coupling. Major principles and governing equations of the two methods (CFD and DEM), in conjunction with their coupling have been described elsewhere (Zhao & Shan, 2013), and are presented in the Appendix.

### Model validation

The CFD and DEM methods adopted in this study were first validated against four relevant and classical problems – namely, glass spheres impacting a rigid barrier (Choi *et al.*, 2020), pure water flow impacting a rigid barrier (Jóhannesson *et al.*, 2009), a single spherical particle falling into the water from the air (Zhao & Shan, 2013) and a particle in free fall (Zhao *et al.*, 2014).

*Verification of DEM: glass spheres impacting a rigid barrier.* In view of the relevance, the DEM simulation in this study was validated against the results of two flume tests by Choi *et al.* (2020); these simulated glass spheres impacting a rigid barrier at different inclination angles of the flume (i.e.  $\theta = 25^\circ$  and  $35^\circ$ ). All the geometries simulated in DEM are identical to those in the flume tests, as detailed by Choi *et al.*

(2020). Parameters related to the mechanical and contact behaviour of the glass sphere (e.g. coefficient of restitution, coefficient of friction and particle density) are summarised in Table 1. Figs 1(a) and 1(b) show the comparison between the measured and computed development of normalised impact force with time for a flume with inclination angles of  $25^\circ$  and  $35^\circ$ , respectively. In both figures, the instantaneous impact force ( $F_i$ ) is normalised by the static load ( $F_s$ ) acting on the barrier. The computed evolutionary trends of impact force with time show reasonable agreement with the results of the two flume tests. Taking the flume test with inclination angles of  $25^\circ$  as an example, the percentage differences between the measured and computed peak impact force is up to 11%, while the computed static impact forces differ from the measured results by only 2%.

### Verification of CFD: water flow impacting the rigid wall.

The design of dams in the run-out zones of avalanches has been a problem of interest for a long time. Jóhannesson *et al.* (2009) investigated the characteristics of impact load of incompressible flow against dams, and proposed theoretical considerations. The impact load is found to be related to flow depth  $h$ , flow density  $\rho$ , flow width  $w$ , gravitational acceleration  $g$  and flow velocity  $v$  (as illustrated in Fig. 2)

$$F = \alpha \rho v^2 h w + \rho g w \frac{h^2}{2} \quad (1)$$

where  $\alpha$  is the dynamic pressure coefficient;  $h$  is taken as the maximum height of the flow that passes through the location of the barrier (Choi *et al.*, 2020); and the velocity  $v$  is taken as the average velocity of the flow front at the moment immediately before impacting the barrier (Choi *et al.*, 2020). Flow density is calculated according to  $\rho = v_s \rho_p + (1 - v_s) \rho_f$  (Zhao & Shan, 2013), where  $v_s$  is the solid fraction;  $\rho_p$  and  $\rho_f$  are the density of particle and fluid, respectively. Jóhannesson *et al.* (2009) suggests an  $\alpha$  value of 1.0 for water impacting a wall. If  $Fr$  is not less than 2.5, the hydrostatic component on the right side of equation (7) can be disregarded. This hydrodynamic model is commonly used to evaluate the peak impact force ( $F_{max}$ ) on the dams.

The CFD method adopted in this study is validated against water impact tests based on the theoretical considerations of Jóhannesson *et al.* (2009). Flume tests are simulated using the CFD to model the interaction between water and the rigid wall. The length, width and depth of the flume are 1.0, 0.2 and 0.5 m, respectively. Five typical channel inclinations are considered – namely, 5, 10, 15, 20 and  $25^\circ$ . In each simulation, pure water is generated at the top of the flume, with a total volume of  $0.006 \text{ m}^3$ . The viscosity and density of water are  $1 \times 10^{-3} \text{ Pa s}$  and  $1.0 \text{ g/cm}^3$ , respectively. Fig. 3 compares the computed values of peak impact force

**Table 1. Input parameters for the DEM simulation of dry granular flow impacting on the barrier (Choi *et al.*, 2020)**

Parameters	Values
Barrier Young's modulus: Pa	$3.2 \times 10^9$
Particle Young's modulus: Pa	$6 \times 10^{10}$
Coefficient of restitution	0.78
Particle density: $\text{kg/m}^3$	2550
Gravitational acceleration: $\text{m/s}^2$	9.81
Inter-element friction coefficient	0.48
Interface-element friction coefficient	0.4
Particle diameter: mm	10
Particle Poisson's ratio	0.25
Barrier Poisson's ratio	0.35

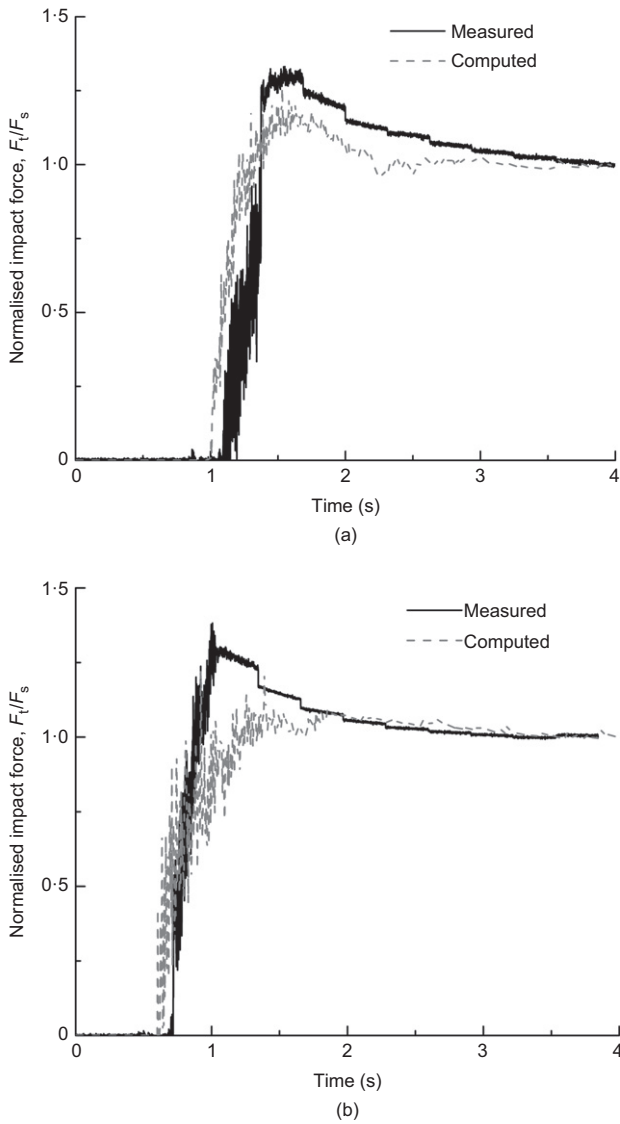


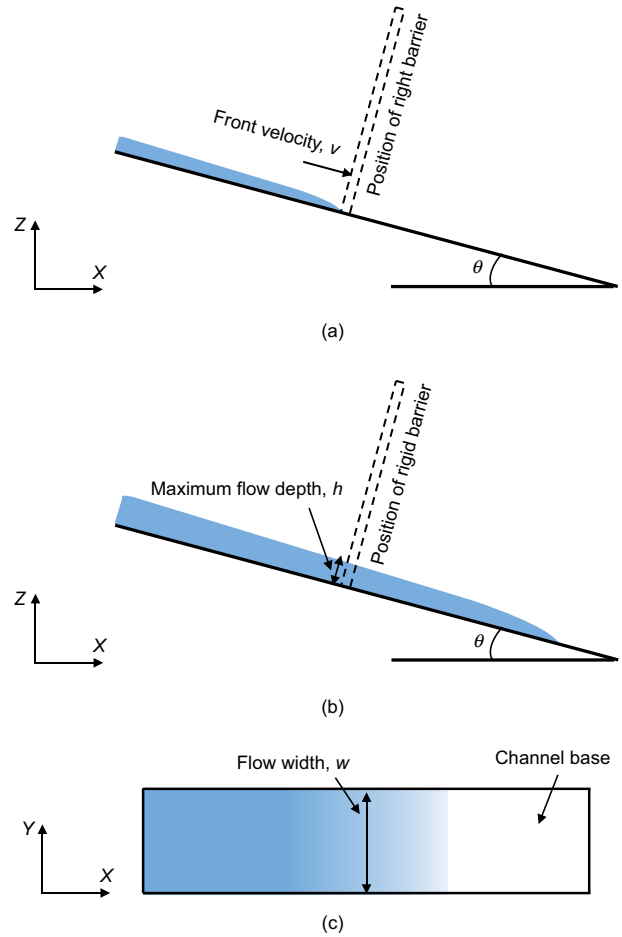
**Fig. 1.** Comparison of computed and measured impact force for barrier with different slope angle: (a)  $\theta = 25^\circ$ ; (b)  $\theta = 35^\circ$

and that calculated based on the theoretical consideration of Jóhannesson *et al.* (2009) and their recommended  $\alpha$  value (i.e.  $\alpha = 1$ ). As can be seen, the computed peak impact forces agree reasonably well with the theoretical results of Jóhannesson *et al.* (2009), with a maximum percentage difference not exceeding 12%. This demonstrates the predictive ability of the CFD adopted in this study for the water impact test in a flume.

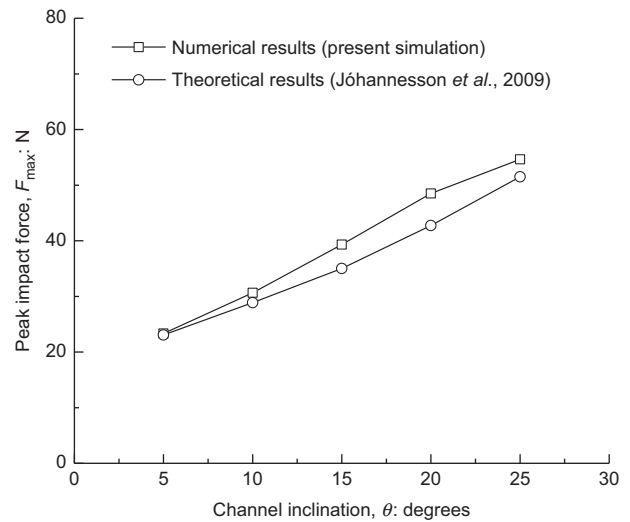
*Verification of CFD–DEM: single particle falling into water from the air.* The validity of the CFD–DEM approach employed in this study was examined through the classical problem of a single particle falling into water from the air. The analytical solution for predicting the settling velocity ( $\mu_p(t)$ ) of a particle into water at any given time ( $t$ ) was well established by Stokes (1844), as follows

$$\mu_p(t) = \frac{1}{18} \frac{(\rho_p - \rho_f) d_p^2 g}{\mu_f} \left[ 1 - \exp\left(-\frac{1}{27} \frac{\mu_f}{\rho_p d_p^2} t\right) \right] \quad (2)$$

where  $\mu_f$  is the fluid viscosity;  $d_p$  denotes the diameter of the particle;  $\rho_p$  and  $\rho_f$  are the density of particle and fluid, respectively; and  $g$  is the acceleration of gravity.



**Fig. 2.** Definition of flow parameters: (a) and (b) elevation, (c) plane view

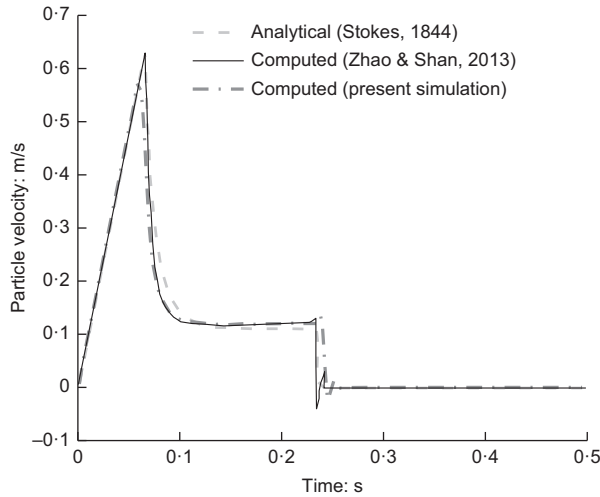


**Fig. 3.** Comparison of the CFD prediction and the theoretical results for water flow impacting the wall

The geometries of the problem, and the parameters related to the water and the particle adopted in the CFD–DEM modelling, are identical to those reported by Zhao & Shan (2013) for simulating the same problem, as summarised in Table 2. Fig. 4 compares the computed and the calculated (by equation (7)) results. It is evident that the computed results by the CFD–DEM modelling have captured the entire process well, including the hitting of the particle on the water surface,

**Table 2. Input parameters for CFD–DEM simulation of single spherical particle settling from air to water (Zhao & Shan, 2013)**

Parameters	Values
Young's modulus: Pa	$5 \times 10^6$
Coefficient of restitution	0.78
Gravitational acceleration: $\text{m/s}^2$	9.81
Particle diameter: mm	1
Poisson's ratio	0.45
Coefficient of restitution	0.3

**Fig. 4. Comparison of the CFD–DEM prediction and the analytical solution for a single particle settling in water**

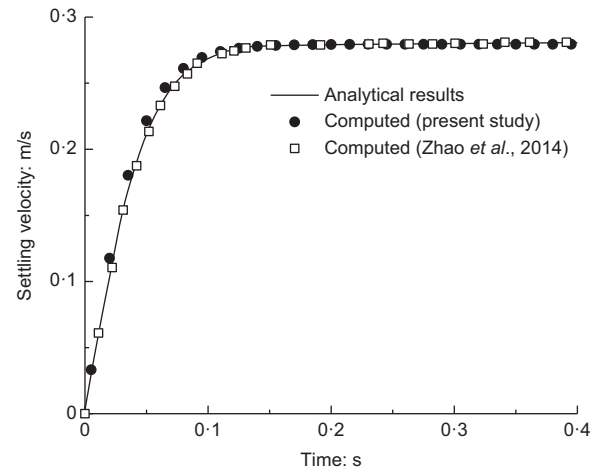
its settling in water and the subsequent bouncing back after hitting the bottom of the container.

*Verification of CFD–DEM: a particle in free fall.* The CFD–DEM approach is further validated by simulating a particle in free fall – that is, a spherical particle with radius of 1 mm settling from a position of 90 mm below the upper surface of the fluid model. This case has been quantified analytically, and computed numerically by way of CFD–DEM coupling by Zhao *et al.* (2014). The motion of a spherical particle in free fall within a fluid can be analytically expressed as (Zhao *et al.*, 2014)

$$\frac{\partial U_r}{\partial t} = \frac{\rho_p - \rho_f}{\rho_p} \mathbf{g} - \frac{3\rho_f C_d U_r^2}{8\rho_p r} \quad (3)$$

where  $U_r$  is the relative settling velocity between the particle and the fluid;  $C_d$  is the drag force coefficient;  $r$  denotes the radius of the particle;  $\rho_p$  and  $\rho_f$  are the density of particle and fluid, respectively; and  $\mathbf{g}$  is the gravitational acceleration.

The geometries of the problem, and the parameters of the fluid and the particle adopted in the CFD–DEM modelling, are identical to those reported by Zhao *et al.* (2014). Fig. 5 shows the computed settling velocity with time by the CFD–DEM approach in this study. The relevant results reported by Zhao *et al.* (2014), including computed results by their CFD–DEM modelling and analytical solution, are also included in the figure for comparison. The computed results by the CFD–DEM approach adopted herein show reasonable agreement with the computed and the analytical results by Zhao *et al.* (2014), with a terminal velocity of the particle equal to 0.28 m/s.

**Fig. 5. The settling velocity of a particle in free fall****Table 3. Programme of numerical simulation**

Test type	Test ID	Solid fraction, $v_s$	Slope angle: deg	Barrier height: m
Dry granular flows	P_0-5	0.5	15	0.6
	P_0-4	0.4		
	P_0-3	0.3		
	P_0-2	0.2		
	P_0-1	0.1		
	WP_0-5	0.5		
Water–particle mixture flows	WP_0-5	0.5	15	0.6
	WP_0-4	0.4		
	WP_0-3	0.3		
	WP_0-2	0.2		
	WP_0-1	0.1		
	WP_0-0	0.0		

## CFD–DEM MODELLING OF DEBRIS FLOW IMPACTING A RIGID BARRIER

### *Objectives and programme of the numerical analysis*

Based on the verified CFD–DEM method, a programme of numerical analyses (see Table 3) was carried out to simulate water–particle mixture flows sliding along a channel to impact a rigid barrier, with the aim of understanding the role of fluid–particle interaction in the mobility of the flow, and its impact against the barrier. In the programme, water–particle mixture flows with a broad range of solid volume fraction,  $v_s$  (i.e. ratio of the solid volume to the global volume of the packing), were considered, to regulate the extent of solid–particle interaction. According to Iverson & George (2014), the solid fractions of saturated debris flows are usually smaller than 0.8 in a flowing state. In this numerical investigation, six values of solid volume fraction  $v_s$  are adopted, namely, 0, 0.1, 0.2, 0.3, 0.4 and 0.5, which cover the range from water flow to hyperconcentrated flow (Pierson, 2005) and debris flow.

Each water–particle mixture flow was calibrated by varying the sliding distance (before hitting the rigid barrier) to enable the same Froude number ( $Fr = 4.0$ ), which is a key dimensionless parameter governing the flow impact on a structure (Hübl *et al.*, 2009; Armanini *et al.*, 2011) and ranges between 0.5 and 7.6, as revealed from field observations (Scheidl *et al.*, 2013; Cui *et al.*, 2015). For comparative purpose, five reference analyses on dry flow with the same Froude number and the corresponding values of  $v_s$  (0.1 to 0.5) were also performed, as summarised in Table 3. For each scenario, two typical inter-particle frictional coefficients ( $\mu = 0.1$  and 0.48) are considered.

### Numerical model set-up, boundary condition and modelling procedure

Figure 6 shows the set-up and geometries of a typical CFD–DEM model simulating water–particle mixture flow (with  $v_s = 0.5$ ) impacting a rigid barrier. A flume model is considered, with its length, width and depth equal to 3, 0.3 and 0.6 m, respectively. The total volume of the hopper (for initial deposition of either water–particle mixture flow, or dry granular flow) at the top of the flume is  $0.045 \text{ m}^3$ . The location of the rigid barrier is case specific, as it has to enable a constant Froude number of 4 in all the cases simulating flows with different solid volume fractions and compositions.

As shown in the figure, the simulation domain is confined within six boundaries – that is, B1 to B6. The boundaries B1, B2, B3, B4 and B6 are rigid, frictional walls for the particles in the DEM domain, and they serve as no-slip walls (i.e. zero hydraulic gradient normal to the wall and zero velocity) in the CFD domain. Meanwhile, no restriction is imposed to the upper atmosphere boundary B5, such that particles in the DEM domain and water in the CFM domain could exit from the boundary freely.

In each numerical analysis, the soil particles were simulated as 10 mm dia. glass spheres, which have often been used in flume model tests (Zheng *et al.*, 2018; Choi *et al.*, 2020), so that their mechanical and contact properties have been well

calibrated (Ng *et al.*, 2017b; Cui *et al.*, 2018). Prior to each simulation, a gravitational acceleration of  $9.81 \text{ m/s}^2$  is applied to the entire computational domain and elements. The particles are then randomly generated in a pre-defined area, and then dumped into the hopper, which is retained by a gate wall (as shown in Fig. 6). Subsequently, water (only for the cases simulating water–particle mixture flow) is added to the hopper to saturate all the void space that has not been occupied by solid particles. After the initial deposition of the flow material in the hopper, the flume is rotated clockwise by an angle of  $15^\circ$ . Until this moment, only the CFD fluid cells in the initial deposition domain are set to contain water, while the remaining fluid cells are fully occupied by air. Finally, the gate wall is deactivated to release the flow, which slides along the slope channel to hit the rigid barrier.

In each analysis, the particles are randomly generated, then fall into the hopper under gravity. To evaluate the homogeneity of the stabilised packing, Fig. 7 shows the initial contact force net (after deposition) for a typical water–particle mixture flow with  $v_s = 0.2$ . No predominating orientation of the force chains appears to exist. To quantify the degree of fabric anisotropy, the deviator fabric ( $\phi$ , as defined by Thornton (2000)) is calculated for the initial deposition of each case simulated in this study, as summarised in Table 4. It can be seen that the initial values of  $\phi$  for the samples (i.e.

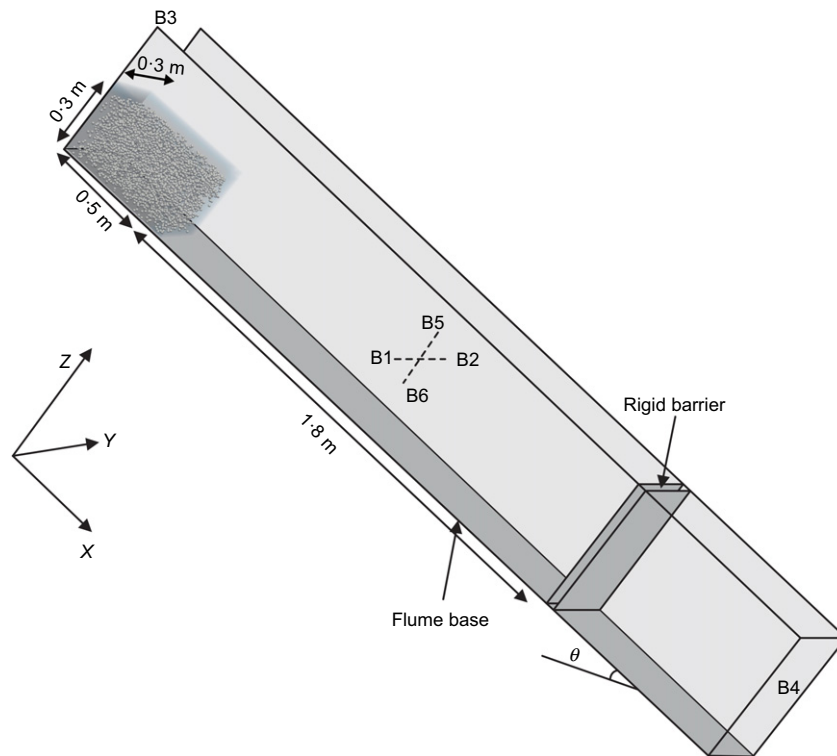


Fig. 6. Numerical model set-up for a typical CFD–DEM simulating water–particle mixture flow (with  $v_s = 0.5$ )

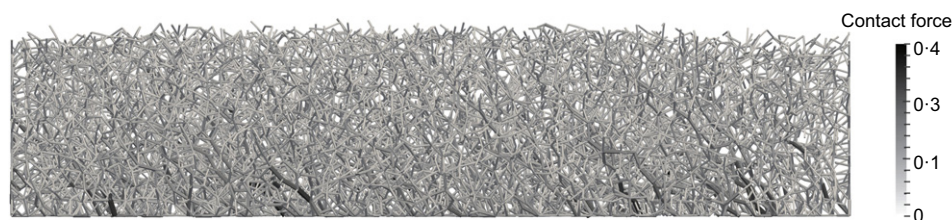


Fig. 7. Contact force net in the initial state for a typical water–particle mixture flow (with  $v_s = 0.2$ )

**Table 4. Initial deviator fabric of each case**

Solid fraction	Initial deviator fabric	
	Dry granular flow	Water–particle mixture flow
0.1	0.053	0.061
0.2	0.068	0.082
0.3	0.074	0.084
0.4	0.075	0.083
0.5	0.075	0.092

particle–water mixture and dry granular mass) simulated in this study are all relatively small (between 0.053 and 0.092), suggesting the initial depositions are like to be homogeneous.

#### Parameters for the particle and the fluid

The particle system is calculated by DEM (Barreto & O’Sullivan, 2012; O’Sullivan *et al.*, 2013). Most of the parameters of the glass spheres (including the coefficient of restitution, particle Poisson’s ratio) have been measured and reported (Cui *et al.*, 2018), as summarised in Table 1. The interface–element friction coefficient of the glass sphere is 0.4, which was measured by means of tilting tests (Pudasaini & Hutter, 2007). With these known parameters, the inter-particle friction coefficient of the glass spheres was obtained by calibrating the DEM modelling against the results of the two flume tests by Choi *et al.* (2020), which simulated glass spheres impacting a rigid barrier at flume inclination angles of 25° and 35°. Details of the flume tests are given by Choi *et al.* (2020), while the model calibration is presented in the earlier section entitled ‘Verification of DEM: glass spheres impacting a rigid barrier’ of this study. The calibrated inter-particle friction coefficient of the glass spheres is 0.48. Other parameters used in the DEM simulation are summarised in Table 1. The fluid phase is simulated by CFD. The viscosities of the water and air are  $10^{-3}$  Pa s and  $1.48 \times 10^{-5}$  Pa s, respectively. The adopted input parameters for CFD–DEM are summarised in Table 5.

## INTERPRETATION OF THE COMPUTED RESULTS

### Distinct impact mechanisms of single- and two-phase flows

Figures 8(a)–8(c) show the computed impact kinematics at three typical moments of a typical dry granular flow (with  $v_s = 0.5$ ), where the initial solid fraction  $v_s$  in the hopper is

**Table 5. Model parameters adopted for CFD–DEM simulations**

Material type	Parameters	Values
Particle	Barrier Young’s modulus: Pa	$3.2 \times 10^9$
	Particle Young’s modulus: Pa	$6 \times 10^{10}$
	Coefficient of restitution	0.78
	Particle density: $\text{kg/m}^3$	2550
	Gravitational acceleration: $\text{m/s}^2$	9.81
	Inter-element friction coefficient: dimensionless	0.48
	Interface-element friction coefficient	0.4
	Particle diameter: mm	10
	Particle Poisson’s ratio	0.25
	Barrier Poisson’s ratio	0.35
Water	Viscosity: Pa s	$1 \times 10^{-3}$
	Density: $\text{kg/m}^3$	$1 \times 10^3$
Air	Viscosity: Pa s	$1.48 \times 10^{-5}$
	Density: $\text{kg/m}^3$	1.0

0.5. In each figure, the captured motion profile and its corresponding velocity vector are shown on the left and the right, respectively. The flow directions are from the left to the right. It can be seen that, after impacting the barrier, the great majority of the dry granular flow deposits at the base of the barrier, except that a few particles bounce back. The flow materials continue to pile up, forming a dead zone (Gray *et al.*, 2003). The stabilised particles serve as a cushion that impedes the flow of subsequent particles. As particles continuously impact the barrier, the size of the dead zone increases progressively. In summary, the dry granular flow simulated in this study shows a typical pile-up mechanism while impacting the barrier.

For comparative purposes, Fig. 9 shows the computed evolving impact kinematics of a typical water–particle mixture flow (with  $v_s = 0.5$ ). This two-phase flow has the same initial solid fraction (with  $v_s = 0.5$ ) and the same Froude number ( $Fr = 4.0$  immediately before impacting the barrier) as those of the dry granular flow shown in Fig. 8. Unlike the dry granular flow (i.e. pile-up mechanism), the water–particle mixture flow simulated with the given parameters exhibits a clear upward jet after the impact, suggesting a run-up mechanism. Upon reaching the maximum run-up height, the two-phase flow begins to roll back and pile up at the base of the barrier. A stagnant dead zone is formed with particles continually depositing at the base of the rigid barrier. In view of the different impact mechanisms observed from the water–particle mixture flows and the dry granular flow, no quantitative comparison is made in this paper. In addition, it is worth noting that the jet-like mechanism is not a unique feature of saturated granular flows, but can also be observed in dry granular flow impacts, depending on factors including the front inclination (Calvetti *et al.*, 2019) and friction (Calvetti *et al.*, 2017).

By comparing Figs 8 and 9, it can be seen that the dry granular flow exhibits a lower mobility and thus a lower run-up height, than that of the water–particle mixture flow with the same  $Fr$  number. This implies that, immediately before impacting the barrier, the latter is likely to have higher kinematic energy than the former, due to less energy dissipation during the sliding of the latter flow. Evidence from the mesoscopic perspective is given later, in the subsequent sections.

### Development of dynamic impact force against the rigid barrier

Figure 10(a) compares the development of dynamic impact force (against the rigid barrier) of dry granular flows having three typical initial solid fractions ( $v_s = 0.1, 0.2, 0.5$ ) but the same Froude number ( $Fr = 4.0$  immediately before impact). The impact force of each flow is normalised by the static load of the dry granular flow with  $v_s = 0.1$ . After the impact of each dry granular flow against the rigid barrier, the impact force keeps increasing, but at a decreasing rate, until reaching a static level. In other words, the peak impact force of each dry granular flow is closed to the final static force due to the self-weight of the dry mass resting on the rigid barrier. This is fundamentally linked to the pile-up mechanism (Song *et al.*, 2017), which may be case specific and dependent on the adopted parameters, for example, front inclination (Calvetti *et al.*, 2019) and friction (Calvetti *et al.*, 2017), rather than being universally valid for dry granular flows. Comparison between the dry granular flows with different  $v_s$  suggests that the flow with a larger solid fraction has led to higher peak impact force, but at a more delayed moment. The delayed occurrence of peak force in a flow with a larger solid fraction is because it involves more inter-particle contacts and shear interactions between particles

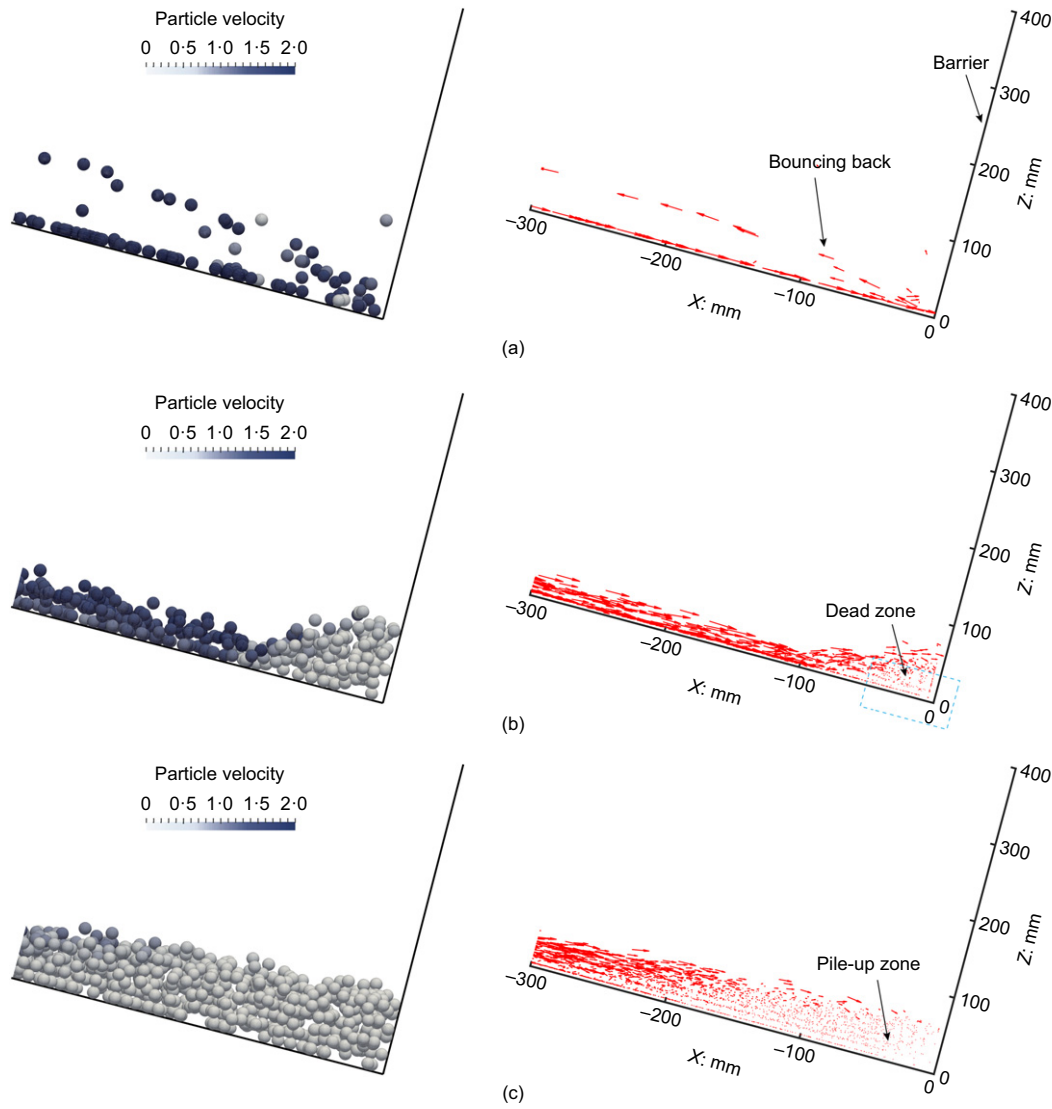


Fig. 8. Computed impact kinematics of test P\_0.5 (all dimensions in mm): (a)  $t = 0$  s; (b)  $t = 0.60$  s; (c)  $t = 1.20$  s

(Choi *et al.*, 2015b). Consequently, lower mobility and loading rates develop on impact.

Figure 10(b) illustrates the development of the dynamic impact force of three typical water–particle mixture flows, with the same Froude number ( $Fr = 4.0$  immediately before impact) and initial solid fractions ( $v_s = 0.1, 0.2, 0.5$ ) as those of the dry granular flows in Fig. 10(a). The impact force of each water–particle mixture flow is normalised by the static load of the dry granular flow with  $v_s = 0.1$ , for a consistent interpretation as in Fig. 10(a). Differing from the dry granular flows, the impact force of each water–particle mixture flow first exhibits a rapid increase until reaching a peak, then dramatically reduces to a final static force (due to the self-weight of the dry mass resting on the rigid barrier). Another difference between the water–particle mixture flow and the dry granular flow is that, after the peak impact, the impact force of the former fluctuates significantly before reaching the final static force. As illustrated in the inset b1 of Fig. 10(b), each impact force reduction during the fluctuation is attributed to the fact that the fluid phase segregates from the mixture and rolls back towards subsequent flow. It is anticipated that flows with a lower solid fraction (or higher fluid fraction) generally exhibit more significant fluctuations after reaching the peak force, due to the repeated impact and rolling back of the water. Similar observations have also been made by Calvetti *et al.* (2017) based on their DEM analyses,

which reveal that the impact–time curves for a granular mass with lower inter-particle friction are more irregular, owing to the reduced energy dissipation.

Comparison between Figs 10(a) and 10(b) shows that, at a given solid fraction, the peak impact force of the water–particle mixture flow is much larger than that of the dry granular flow. This implies that more kinetic energy is accumulated in the water–particle mixture flows. Detailed discussion from the mesoscopic perspective is given later, in subsequent sections. It should also be noted that the peak impact forces, for both saturated and dry granular flows, are related to the impact mechanism. To be more specific, for any flow that exhibits a pile-up mechanism, the peak impact force is equal to the final static force. In contrast, for either saturated or dry granular flow that shows a run-up (or jet-like) mechanism, the peak impact force should be higher than the final static force (Calvetti *et al.*, 2016, 2019).

It is a routine practice to estimate the dynamic impact force ( $F$ ) using equation (7) (as given in the earlier section entitled ‘Verification of CFD: water flow impacting the rigid wall’), which was proposed based on the hydro-dynamic approach (Jóhannesson *et al.*, 2009; Kwan, 2012). Based on the computed impact forces in Fig. 10 and equation (7), the dynamic pressure coefficient values  $\alpha$  of all cases were back-calculated, and they are plotted in Fig. 11. All the parameters needed in equation (7) are summarised in Table 6.

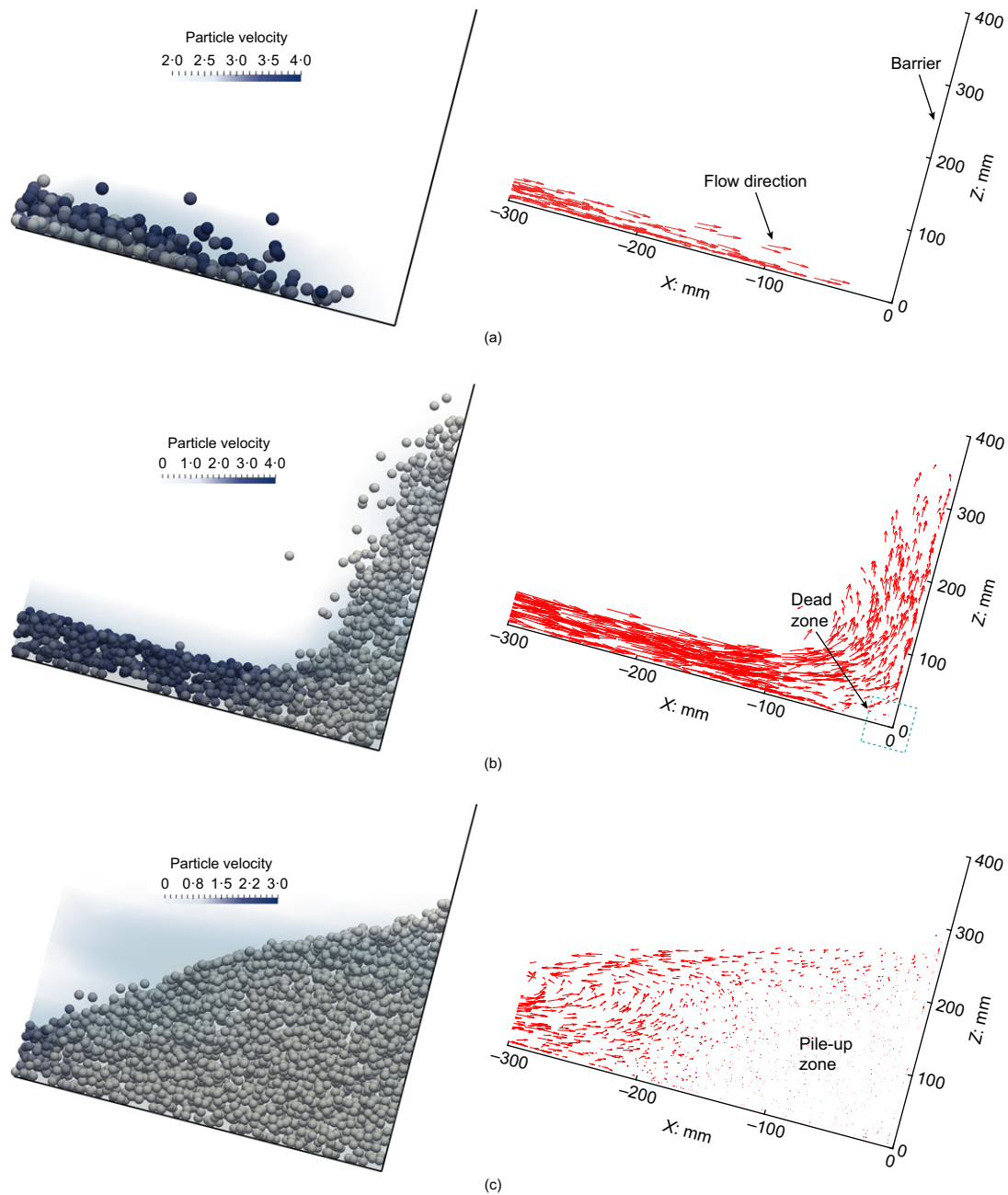


Fig. 9. Computed impact kinematics of test WP\_0-5 (all dimensions in mm): (a)  $t = 0$  s; (b)  $t = 0.33$  s; (c)  $t = 0.80$  s

Two reference lines for  $\alpha$  – namely,  $\alpha = 1.0$  for incompressible fluid impacting a wall (Jóhannesson *et al.*, 2009) and  $\alpha = 2.5$  for a water–particle mixture flow against a rigid barrier (Kwan, 2012) – are also included in the figure.

As illustrated, the dynamic pressure coefficient  $\alpha$  varies significantly among the cases simulated in this study – that is, it ranges between 0.07 and 2.83, depending on the presence of the fluid phase and the solid fraction. For each given solid fraction, the  $\alpha$  value of the water–particle mixture flow (i.e. predominated by the run-up mechanism) is much larger than that of the dry granular flow (i.e. predominated by the pile-up mechanism), with a difference of up to about 16 times. By contrast, except for pure water flow ( $v_s = 0$ ), the increase in solid fraction has led to a reduction in the value of  $\alpha$ . Although the dynamic pressure coefficient values  $\alpha$  decrease with increasing solid fraction  $v_s$  for water–particle mixture flow (except pure water flow ( $v_s = 0$ )), the peak dynamic impact load does not occur in the case with the smallest one  $v_s$  (i.e. 0.1), but in the case with  $v_s = 0.2$ . This is likely to be

because the peak dynamic impact load depends on the interplay between  $\alpha$  (decreasing with increasing  $v_s$ ) and density (increasing with  $v_s$ ), as readily described by the empirical equation of Jóhannesson *et al.* (2009) (see equation (7)) and the new design formula proposed by Calvetti *et al.* (2019). Figs 10(a) and 10(b) also suggest that the fluctuation of the impact–time curve can be more pronounced when there are fewer inter-particle interactions, owing to smaller energy dissipation during sliding (Calvetti *et al.*, 2017). This can be achieved by either introducing fluid or reducing the number of particles in the flow.

Alternatively, the same results can also be achieved by reducing friction – for example, friction (among grains or grain–ground). The effect of the friction coefficient on the dynamic impact was investigated by running four additional numerical simulations on dry granular flow with different inter-particle friction coefficients ( $\mu = 0.1, 0.3, 0.48, 0.6$ ) but the same Froude number ( $Fr = 4.0$ ) and identical volumetric solid fraction ( $v_s = 0.2$ ). Fig. 12 compares the dynamic

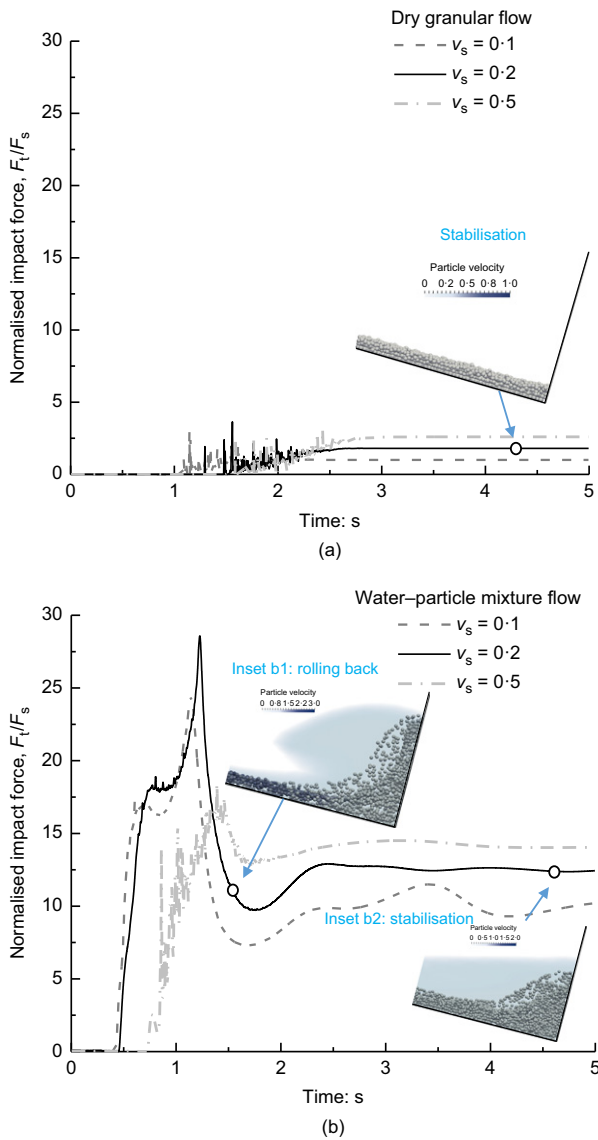


Fig. 10. Computed impact force–time history: (a) dry granular flow; (b) water–particle mixture flow

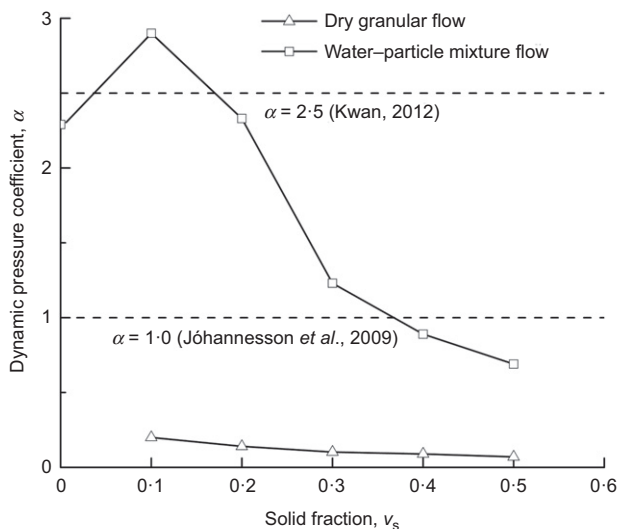


Fig. 11. Comparison of dynamic pressure coefficient of water–particle mixture flows and dry granular flows with  $v_s$  varying from 0.0 to 0.5

impact of these four dry granular flows impacting a rigid barrier. Micromechanical interpretations of the flows during impact instants of two typical cases ( $\mu = 0.1$  and  $0.6$ ) are also given by showing the impact kinematics in the inset of the figure. It can be seen that an increase of  $\mu$  from  $0.1$  to  $0.6$  has led to a percentage reduction of the peak impact load by  $64\%$ , due to the intensified energy dissipation during the propagation of flows with higher  $\mu$ . In particular, the friction plays an important role in altering the impact mechanisms (see the inset of Fig. 12) from the run-up mechanism for the low-friction case ( $\mu = 0.1$ ) to the pile-up mechanism for cases with relatively high friction ( $\mu = 0.3, 0.48, 0.6$ ). This confirms that the run-up (or jet-like) mechanism can also occur in dry granular flow impacts, depending on factors such as friction (Calvetti *et al.*, 2017).

Differing from the observations in this study (i.e. peak impact load decreasing with  $\mu$ ), Calvetti *et al.* (2017) found the peak impact load increased with  $\mu$  based on their DEM analysis of dry granular flow impacting a rigid barrier. Quantitatively, the peak impact load of the dry flow with  $Fr = 2.41$  increased by  $44\%$  when  $\mu$  increased from  $0.1$  to  $0.5$  (Calvetti *et al.*, 2017). The opposing trends observed in this study and the simulations of Calvetti *et al.* (2017) are likely to be due to the different modelling techniques adopted in the two studies. The former simulates both propagation and impact phases, while the latter ignores the propagation and simulates only a granular flow with a pre-defined initial velocity at the time instant just preceding the impact. In other words, the peak impact load in the latter analyses was rarely influenced by the dissipation, but mainly affected by elastic properties of the mass, which increases with  $\mu$  (Calvetti *et al.*, 2017).

To explore the effect of the initial deposition (particularly the fabric effect), a preliminary comparative study was performed. Two CFD–DEM simulations were carried out on particle–water mixtures having the same Froude number  $Fr = 4.0$  and volumetric solid fraction  $v_s = 0.2$ , but two different values of deviator fabric, namely  $0.082$  and  $0.009$ . The former resulted from natural one-dimensional (1D) deposition of glass spheres with the inter-particle friction coefficient of  $0.48$  (identical to other analyses simulated in this study) under gravity. The latter was achieved by the following procedures according to Yimsiri & Soga (2010)

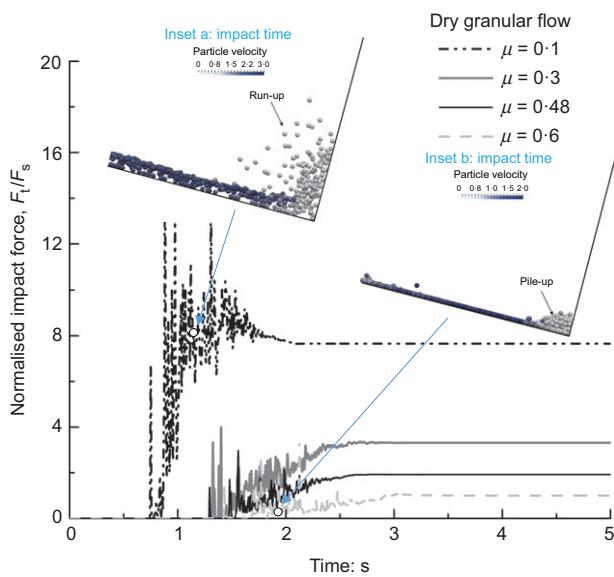
- rendering natural 1D deposition of the glass spheres with the inter-particle friction coefficient of  $0.00$  into the hopper
- compressing the glass spheres with a vertical stress  $30$  kPa
- increasing the inter-particle friction coefficient between glass spheres to  $0.48$
- releasing the vertical stress of the glass spheres.

After preparation of the two water–particle mixtures with different deviator fabric ( $\phi = 0.082$  and  $0.009$ ), the gate wall of the hopper in each case was deactivated to release the flow for the impact tests.

Figure 13 compares the development of the dynamic impact force of water–particle mixture flows with the same Froude number ( $Fr = 4.0$  immediately before the impact) and the volumetric solid fraction ( $v_s = 0.2$ ), but different deviator fabric ( $\phi = 0.082$  and  $0.009$ ). The evolution of the dynamic impact force against the rigid barrier does not appear to be noticeably affected by the initial deposition. This is because the initial deviator fabric had been completely destroyed along with the collapse and initiation of flow of the glass sphere packing, which was triggered by the release of the gate wall.

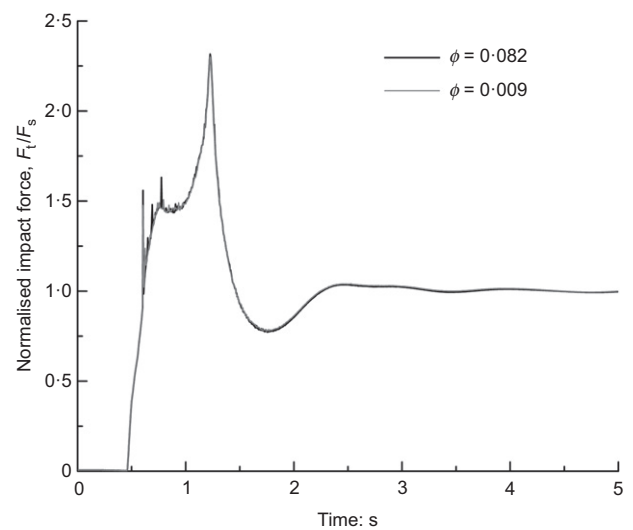
**Table 6. Summary of parameters for calculating the dynamic impact coefficient  $\alpha$** 

Test type	Test ID	Solid fraction, $v_s$	Flow density: kg/m <sup>3</sup>	Maximum flow depth: m	Front velocity: m/s
Dry granular flows	P_0.5	0.5	2550	0.050	3.00
	P_0.4	0.4	2550	0.049	2.74
	P_0.3	0.3	2550	0.036	2.42
	P_0.2	0.2	2550	0.030	2.31
	P_0.1	0.1	2550	0.021	1.71
Water-particle mixture flows	WP_0.5	0.5	1775	0.055	3.05
	WP_0.4	0.4	1620	0.051	3.10
	WP_0.3	0.3	1465	0.049	3.08
	WP_0.2	0.2	1310	0.040	2.75
	WP_0.1	0.1	1155	0.037	2.55
	WP_0.0	0.0	1000	0.060	2.94

**Fig. 12. The influence of inter-element friction coefficient on the dynamic impact of water-particle mixture flow and dry granular flow ( $Fr = 4.0$ ,  $v_s = 0.2$ )**

Otherwise, it can also be seen from Fig. 11 that the dynamic pressure coefficient  $\alpha$  for the case with  $v_s = 0$  (flow with pure water) is approximately 2.3, which is bigger than the recommended  $\alpha$  value (e.g. 1.0) for the impact of an incompressible fluid onto a wall (Jóhannesson *et al.*, 2009). This is because the  $\alpha$  value is closely related to the initial conditions – for example, the volume of water and sliding distance. An increase of  $v_s$  from 0 to 0.1 (by addition of particles into the flow) leads to an increased  $\alpha$  value from 2.3 to 2.83. With further increase of  $v_s$  (from 0.1 to 0.5), however, the  $\alpha$  value keeps decreasing from 2.83 to 0.69. These controversial responses are associated with the two competing roles played by mechanisms introduced through the addition of particles: (a) increasing dynamic impact by raising the overall density of the water-particle mixture, and (b) decreasing dynamic impact by generating more energy dissipation due to inter-particle interaction. The computed results suggest that the former mechanism dominates when  $v_s$  is no larger than 0.1, whereas the latter prevails when  $v_s$  exceeds 0.1.

The recommended dynamic pressure coefficient ( $\alpha = 2.5$ , based on Kwan (2012)) for a rigid barrier is shown to overestimate the  $\alpha$  values of all the cases simulated in this study, except the water-particle mixture flow with a very low solid fraction ( $v_s = 0.1$ ). The computed  $\alpha$  values, particularly for the dry granular flow, are relatively low when compared with those reported in the literature – that is, typically higher

**Fig. 13. The influence of initial deviator fabric ( $\phi$ ) on the dynamic impact of water-particle mixture flow ( $v_s = 0.2$ )**

than 2.0 (Hübl *et al.*, 2009; Scheidl *et al.*, 2013). It is revealed based on DEM analyses that dynamic impact could be significantly affected by the initial condition (Calveti *et al.*, 2019). In this study, the distance between the initiation of the flow and the barrier adopted is relatively long (as evident by the high Froude number = 4.0), resulting in higher energy dissipation during the flow propagation and subsequently a smaller dynamic impact coefficient. Other factors such as the adoption of frictional boundaries, and the computed pile-up mechanism (which intensifies energy dissipation by way of shearing between layers of flow being piled up) could also be responsible for the low  $\alpha$  values of the dry granular flows simulated in this study. The relatively low  $\alpha$  values, however, are unlikely to alter the key conclusions drawn from this comparative study on cases with the same Froude number.

It is worth noting that the quantitative results above may be case-specifically related to the scenarios and parameters considered in this study, which mainly concerns the effect of the volumetric solid fraction  $v_s$ . The change of other parameters such as Froude number, flow velocity, friction among grains and with the ground and grain size distribution is likely to alter the values of  $\alpha$ . In addition, the front inclination has also been identified as an important parameter affecting  $\alpha$  (Hübl *et al.*, 2009; Calveti *et al.*, 2019). It will be the authors' future pursuit to perform a more comprehensive study by considering these effects for investigating and quantifying the  $\alpha$  values of both water-particle mixture flow and dry granular flow.

*Relative contribution of water and particle impact force against the rigid barrier*

One major advantage of the calibrated CFD–DEM models is that they offer the information on the relative contribution of water and particles to the total impact force, which can be rarely obtained in the experimental study. Fig. 14 shows the ratio of impact force caused by water ( $F_w$ ) to the impact force induced by particles ( $F_p$ ) changing with time during the impact of three typical water–particle mixture flows (i.e.  $v_s = 0.1, 0.2$  and  $0.5$ ). In the figure, the initial time ( $t = 0$  s) corresponds to the moment when the particles just come into contact with the rigid barrier.

It can be seen from Fig. 14 that when the volumetric solid fraction is relatively small (i.e.  $v_s = 0.1$  and  $0.2$ ), the water exerts a larger impact load to the rigid barrier than that of the particles (i.e.  $F_w/F_p > 1.0$ ). In particular, for flow with a very low volumetric solid fraction (i.e.  $v_s = 0.1$ ), the dynamic impact force caused by water ( $F_w$ ) is 16 times that caused by particles ( $F_p$ ) upon the initial impact (when  $t = 0$  s). This suggests the initial impact of the water–particle mixture flow with a low  $v_s$  ( $0.1$ ) is mainly governed by the interaction between the water fronts (which segregate from the mixture) and the barrier. The ratio  $F_w/F_p$  then decreases with time when a larger portion of particles impact the barrier, and finally stabilises at a ratio exceeding unity. The ratio of  $F_w/F_p$  decreases as more volumetric fraction of solid is involved. When the volumetric solid fraction  $v_s$  increases to  $0.5$ , the value of  $F_w/F_p$  is approximately equal to  $1.0$  during the entire impacting process, meaning that water and particles exert an approximately identical force to the rigid barrier.

*Water–particle interactions*

To explain the observed distinct impact mechanisms (including impact kinematics and impact forces) observed from the water–particle mixture flows and dry granular flows, as discussed in the preceding sections, the solid–fluid interactions are analysed in this section. The total interaction force exerted on the particle system by the fluid phase, which usually cannot be measured experimentally, has been calculated and further projected onto the  $x$  and  $z$  directions. As defined in Fig. 6, the  $x$  and  $z$  directions are parallel and perpendicular to the slope of the flume, respectively.

Figure 15(a) shows the computed interaction force along the direction parallel to the slope of the flume ( $x$  direction) for three typical water–particle mixture flows with  $v_s = 0.1, 0.2$  and  $0.5$ .

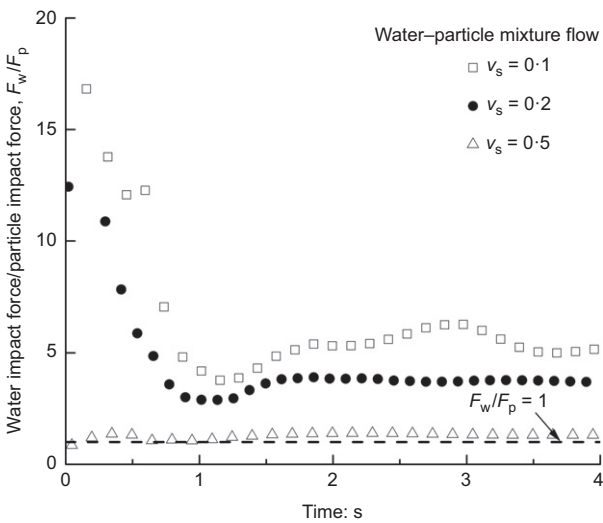


**Fig. 14.** Comparison between water impact force and particle impact force for water–particle mixture flows

$0.2$  and  $0.5$ . In the figure, the time of  $0$  s means the moment when the gate wall (for retaining the flow in the hopper) is about to release. A positive interaction force means the water imposes a driving downward force to enhance the kinematics of the particles, and vice versa. During the first few seconds, positive interaction forces are developed in all three flows, which have not reached the maximum run-up height. The water moves faster than the particles, and thus imposes a downward driving force to accelerate movement of the particle system along the flow direction (see inset a1 in Fig. 15(a)). After the first few seconds, the interaction force in the three flows turns to negative. This is related to the rolling back of the water (see inset a2 in Fig. 15(a)) to resist the particle system which is approaching the barrier.

Figure 15(b) shows the computed interaction force along the direction perpendicular to the slope of the flume ( $z$  direction) for the same water–particle mixture flows analysed in Fig. 15(a). During the entire process involving flow sliding and barrier impacting, the interaction forces along the  $z$  direction remain positive for all the three water–particle mixture flows ( $v_s = 0.1, 0.2$  and  $0.5$ ), due to the buoyancy of the water applied to the particles (see inset b1 in Fig. 15(b)).

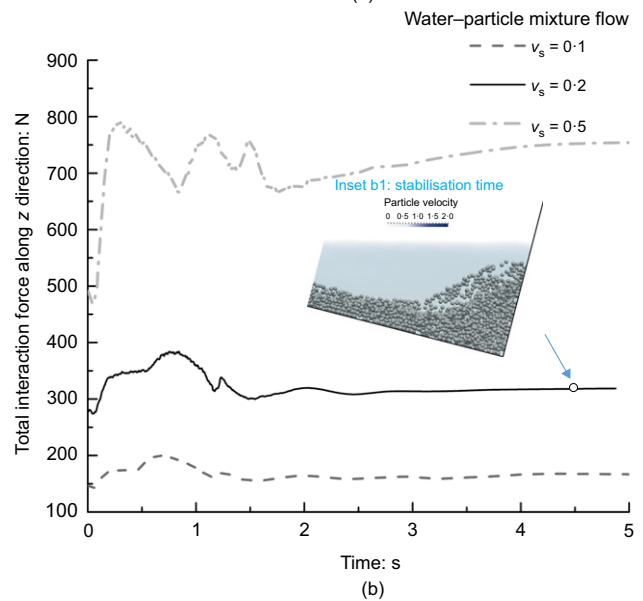
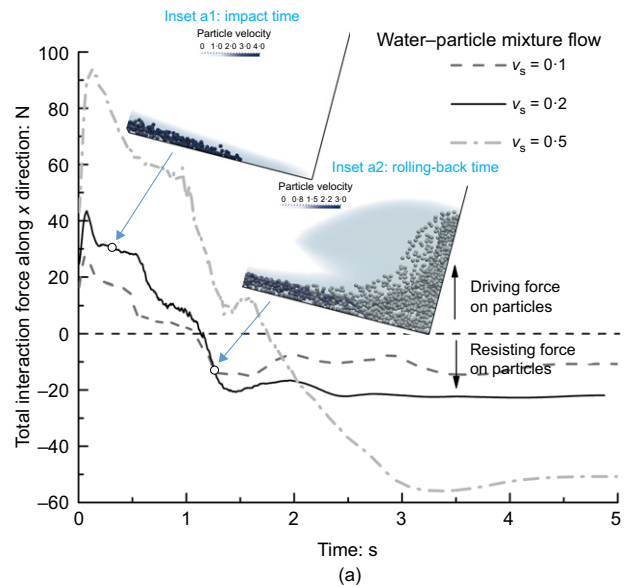


**Fig. 15.** Total interaction force on the particle system from the fluid phase along (a)  $x$  and (b)  $z$  directions

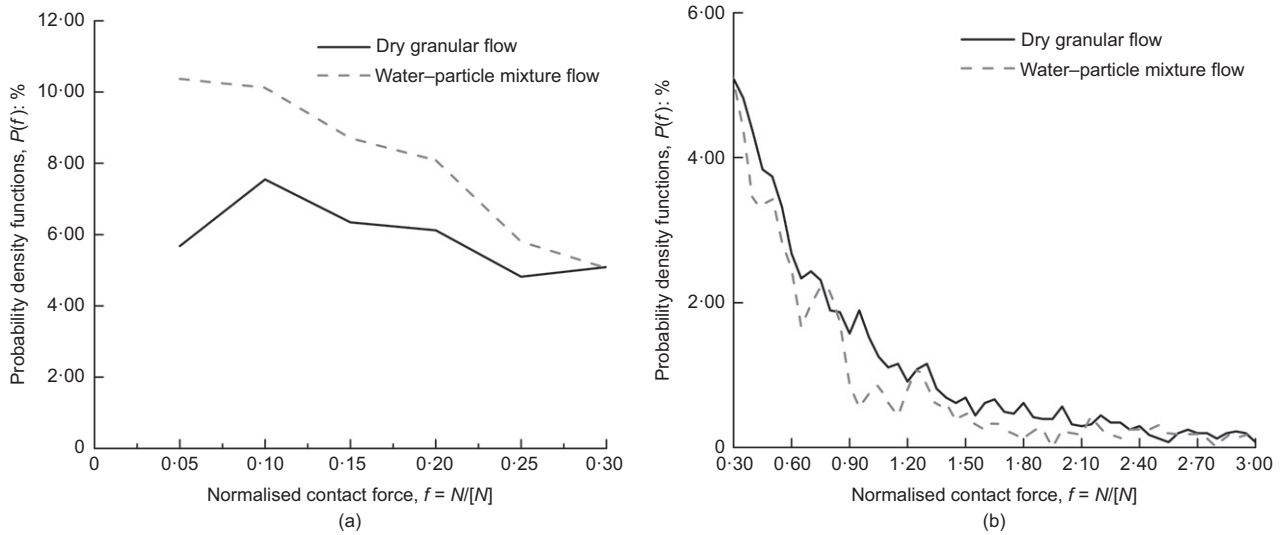


Fig. 16. Probability density functions of inter-particle normalised contact force when particles just reach the barrier with  $v_s = 0.2$

To offer further insights into the influence of fluid on particle interactions, Fig. 16 shows the probabilistic density function of the contact force of a water-particle mixture flow and a dry granular flow having the same  $v_s = 0.2$  at the moment immediately before impacting the barrier. In the figure, the contact force of each particle  $N$  is normalised by the average contact force  $\langle N \rangle$ , – that is, normalised contact force  $f = N/\langle N \rangle$  (Shire & O’Sullivan, 2013). According to Shire & O’Sullivan (2013), strong and weak contact forces may be characterised by the criteria of  $f > 1$  and  $f < 1$ , respectively. It is revealed from the figure that the particles in the water-particle mixture flow have more weak contacts (with  $f < 0.3$ ), but a smaller number of strong contacts ( $f > 1$ ), as compared with those in the dry granular flow. These further reveal the role of the fluid phase in the former flow in exerting buoyant force to reduce the inter-particle contacts.

#### Energy transfer and dissipation

The aim of this section is to understand the influence of water-particle interaction on energy transfer and dissipation, and their consequence in terms of the impact of flow to the rigid barrier. The total energy of the debris flow consists of potential energy ( $E_p$ ) and kinetic energy ( $E_k$ ). The instantaneous potential energy ( $E_p$ ) is calculated by the following equation

$$E_p = \sum_{i=1}^R m_i g h_i + \sum_{j=1}^M m_j g h_j \quad (4)$$

where  $m_i$  and  $h_i$  denote the mass and height of any given particle  $i$ , respectively;  $R$  is the total number of particles;  $m_j$  and  $h_j$  denote the mass and height of water in any given fluid cell  $j$ , respectively;  $M$  is the total number of fluid cells. The second term regarding the potential energy of water is not considered in the calculation for the dry granular flows. The instantaneous kinetic energy ( $E_k$ ) is calculated as follows

$$E_k = \frac{1}{2} \sum_{i=1}^R m_i v_i^2 + \frac{1}{2} \sum_{j=1}^M m_j v_j^2 \quad (5)$$

where  $v_i$  denotes the velocity of any given particle  $i$ ;  $v_j$  is the velocity of water in any given fluid cell  $j$ . For dry granular flow, the second term is not taken into account. The

instantaneous dissipated energy ( $E_d$ ) of each flow can be readily calculated by subtracting  $E_p$  and  $E_k$  from the initial total energy ( $E_i$ )

$$E_d = E_i - E_k - E_p \quad (6)$$

All these energy components can be recorded in the simulation process and then analysed for energy evolution and transformation. Each energy component in a flow is normalised by the initial potential energy ( $E_i$ ). Fig. 17(a) shows the energy evolution of dry granular flow with  $v_s = 0.2$ , from the triggering moment of the flow to the end of its deposition. As is shown, after the trigger of the dry granular flow ( $t = 0$  s), the potential energy progressively transformed into kinetic energy. The kinetic energy shows a peak at about  $t = 1.5$  s, when the potential energy loss rate and the cumulative energy dissipation rate reach the maximum value. This corresponds to the moment when the front of the dry granular flow immediately reaches the barrier (see inset a1 in Fig. 17(a)). After impacting the barrier, both kinetic and potential energy decrease until reaching a static state at around  $t = 3.0$  s (see inset a2 in Fig. 17(a)). A total of 58% of the energy is dissipated during the overall flow process. Two sources of energy dissipation in the dry granular system were determined – namely, the interactions between particles and the interactions between particles and boundary.

Figure 17(b) illustrates the energy transfer of the water-particle mixture flow with  $v_s = 0.2$ , from the triggering moment of the flow to the end of its deposition. Obviously, the kinetic energy exhibits an increasing trend during  $t = 0 \sim 0.58$  s. The increasing rate of kinetic energy of the water-particle mixture flow is larger than that of the corresponding dry granular flow, as shown in Fig. 17(a). This suggests the presence of water in the former flow has led to less energy dissipation during the sliding, owing to the buoyant force (Fig. 17(b)), which reduces the inter-particle contact force (Fig. 16) and thus dissipation occurs through shearing between particles. When the front water runs up the maximum height, the vertical jet begins to roll back to the flume base (see the inset b1 in Fig. 17(b)). During this process, the potential and kinetic energy of the liquid system increases, which even eliminates the loss caused by the particle system, as shown by the constant value of  $E_k$  during the period between 1.07 and 1.18 s. Compared with the dry granular flow, less energy (about 50%) is dissipated when the

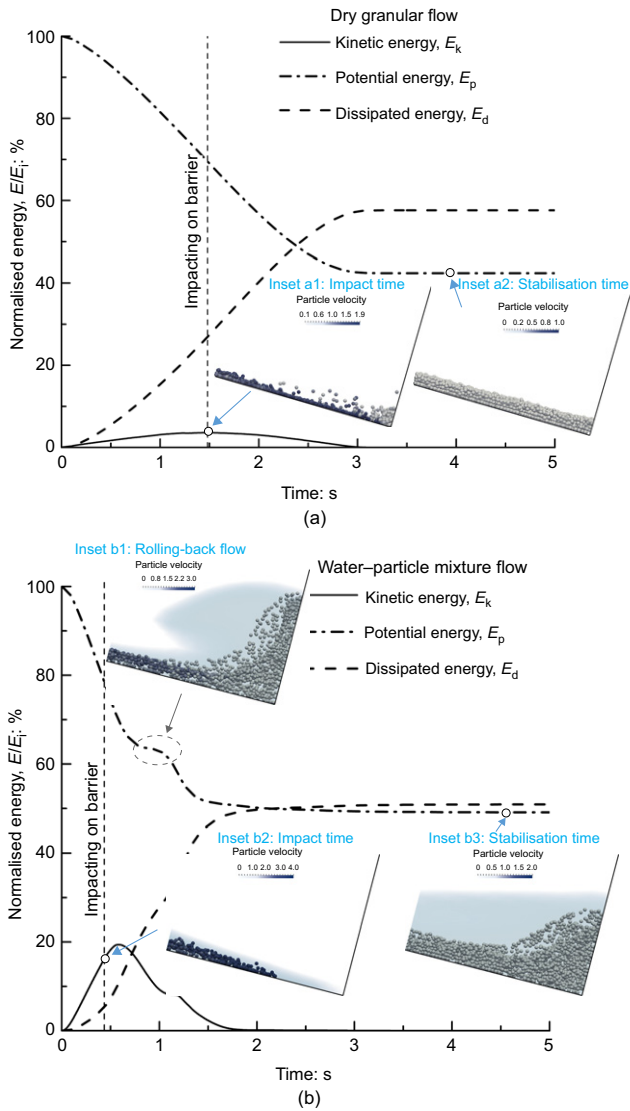


**Fig. 17. Change in normalised energy for  $v_s = 0.2$ : (a) dry granular flow; (b) water–particle mixture flow**

flow comes to an end at around  $t = 1.75$  s (see the inset b2 in Fig. 17(b)). The difference indicates the role of water in facilitating the motion of grains past one another and moderating the interaction between particles, which has been closely explained in the section entitled ‘Water–particle interactions’. For the water–particle mixture flow, the energy dissipated includes five parts: the interactions between particles; the interactions between particles and boundary; the interactions within the liquid phase; the interactions between water and boundary; and the water–particle interactions.

Considering different solid fractions for dry granular flow and water–particle mixture flow, the dissipated energy represented by the total initial energy when the debris flow is just reaching the barrier is plotted in Fig. 18. It can be seen that the higher the solid fraction is, the greater is the proportion of energy dissipated during the flow process (before impacting the barrier). Furthermore, for a given  $v_s$ , the dry granular flow has dissipated more energy than the water–particle mixture, with a maximum difference of 4.5 times. Taking  $v_s = 0.2$  as an example, immediately before impacting the barrier for the dry granular flow, about 28% of the total initial energy is dissipated. The rest of the energy, about 30%, is dissipated during the impact process, which is

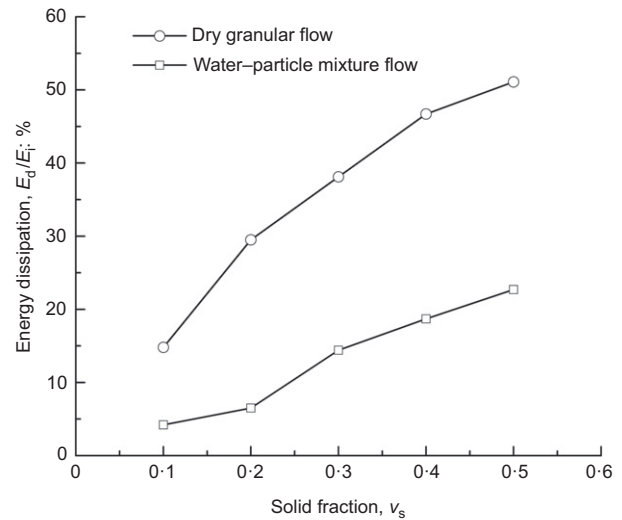


**Fig. 18. Comparison of energy dissipated between flows with different inter-particle frictions before initial impact on barrier**

mostly caused by inter-particle interactions. However, about 6% of the total initial energy in the water–particle mixture flow is dissipated before reaching the barrier, which is far less than that in the dry granular flow. After the impact, about 44% of the total energy is further dissipated, mainly due to the interactions on particles by the fluid phase, which will roll back towards subsequent flow. The differences in Fig. 18 have been explained in preceding sections.

### Discussion

Owing to the page limit, this study focuses only on the effect of volumetric solid fractions on flow and impact of both the water–particle mixture flow and dry granular flow. Nevertheless, there are also other parameters which might have important qualitative and quantitative effects on the flow and the impact – for example, Froude number (Chehata *et al.*, 2003; Hákonardóttir *et al.*, 2003), velocity (Song *et al.*, 2017), friction among grains and with the ground (Choi *et al.*, 2015b; Zhou *et al.*, 2016) and grain size distribution (Cui *et al.*, 2018).

Some preliminary attempts have been made (through additional numerical analyses) to explore whether the qualitative and quantitative results presented in this study would change by choosing different values for the above parameters. It was found that, by varying the aforementioned parameters, the qualitative conclusions for the flow and the impact drawn from this study are not altered – that is, the water–particle mixture flow exhibits a larger run-up and higher impact pressure than the dry granular flow with the corresponding Froude number. This is anticipated, because the two roles played by particle–fluid interaction (i.e. increasing the driving force to particles, and reducing the energy dissipation at inter-particle contacts) always exist, irrespective of flow velocity, inter-particle friction and grain size distribution. In contrast, the quantitative results for the flow and the impact obviously change with these parameters, as expected.

Although this numerical investigation reveals that the presence or absence of water has induced jet-like behaviour (run-up mechanism) or stagnant zones (pile-up mechanism), respectively (see Figs 8 and 9), these observations were case-specifically related to the tests and parameters adopted in this study. Indeed, the run-up mechanism and pile-up mechanism could occur in flows with or without the presence

of water, mainly depending on the kinematics of the flow immediately impacting the barrier. For example, jet-like behaviour (run-up mechanism) was observed from flume tests simulating dry particle flows (consisting of either glass spheres or sand) impacting a rigid barrier (Ng *et al.*, 2017b). This is likely to be associated with the high inclination angle of the flume (40°), which should have intensified the kinematics of the dry particle flow before impacting the rigid barrier, and facilitated run-up of the flow.

## CONCLUSIONS

This paper presents a comparative study based on CFD–DEM modelling of both water–particle mixture flow and dry granular flow impacting a rigid barrier, with the aim of understanding the influence of water–particle interaction on the mobility of debris flow and its impact on a barrier from the mesoscopic perspective. Based on the limited number of cases simulated and the parameters adopted, the conclusions from this study can be summarised as listed below.

- The water–particle mixture flows exhibit a distinct run-up mechanism, while the dry granular flows exhibit a pile-up mechanism. The transition between mechanisms is governed by the fluid phase, which reduces the inter-particle interactions and therefore energy dissipation from shearing among grains. Consequently, compared to the corresponding water–particle mixture flow, dry granular flow with solid fraction  $v_s = 0.5$  exhibits a lower run-up height and a smaller peak impact force.
- The effect of the solid fraction,  $v_s$ , is reflected by the run-up height and static load on the rigid barrier. Higher solid fractions lead to larger and more obvious dead zones, and enhance frictional contacts among grains, which reduces the mobility of a flow. The maximum run-up height of the water–particle mixture flow with  $v_s = 0.5$  is larger compared with water–particle mixture flow with  $v_s = 0.2$ , while the static load applied to the rigid barrier is smaller.
- The mesoscopic insight from CFD–DEM modelling reveals that the particle–fluid interaction plays two roles in increasing the kinematic energy of particles: (i) imposing a driving force to the particles; (ii) reducing the inter-particle contact forces and therefore energy dissipation from shearing among grains by applying buoyancy to the particles.
- While impacting the rigid barrier, most of the energy of the water–particle mixtures (exhibiting a run-up mechanism) is dissipated as the fluid phase segregates from the mixture and rolls back towards subsequent flow. This differs from the conventional impact mechanism observed for dry granular flows, where the energy is mainly dissipated by way of shearing between layers of particles piling up behind a barrier.

All the conclusions above are drawn based on the simulated interaction between Newtonian fluid and particles, and the impact of the particle–Newtonian fluid mixture on a barrier. It will be the authors' future pursuit to investigate the effect of fluid type (such as non-Newtonian liquids including Bingham and Herschel–Bulkley fluids), which was shown to significantly affect the fluid–particle interaction (Li & Zhao, 2018), on the dynamic impact of fluid–particle mixture against a barrier.

## ACKNOWLEDGEMENTS

The authors gratefully acknowledge the financial support from the National Key Research and Development Program (2016YFC0800200), National Natural Science Foundation of China (51779221 and 51939010) and Zhejiang Provincial Natural Science Foundation (2018C03031 and LHZ20E090001). J. Zhao acknowledges the financial support of the Research Grants Council of Hong Kong under projects GRF 16205418, CRF C6012-15G and TBRS T22-603/15N. The valuable comments given by Professors Charles Ng, Clarence Choi and Yifei Cui at The Hong Kong University of Science and Technology are also gratefully acknowledged.

## APPENDIX. COUPLED CFD–DEM MODELLING

### Governing equations for the particles in DEM

The translational and rotational motions of each particle  $i$  are controlled by Newton's equations of motion, which can be written as (Climent *et al.*, 2014; Li & Zhao, 2018)

$$\begin{cases} m_i \frac{dU_i^p}{dt} = \sum_{j=1}^{n_i^c} F_{ij}^c + F_i^f + F_i^g \\ I_i \frac{dw_i}{dt} = \sum_{j=1}^{n_i^c} (M_{t,ij} + M_{r,ij}) \end{cases} \quad (7)$$

where  $m_i$  and  $I_i$  are the mass and moment of inertial of a single particle  $i$ , respectively.  $U_i^p$  and  $w_i$  indicate the translational and angular velocities of particle  $i$ , respectively.  $n_i^c$  is the total number of contacts for particle  $i$ .  $M_{t,ij}$  and  $M_{r,ij}$  are, respectively, the tangential resistant moment and rolling resistant moment acting on particle  $i$  by particle  $j$ .  $F_i^f$  and  $F_i^g$  are the particle–fluid interaction force and the gravitational force, respectively, acting on particle  $i$ .  $F_{ij}^c$  is the contact force acting on particle  $i$  by particle  $j$  or walls, which is calculated based on Hertzian–Mindlin contact model for describing the normal and tangential contact forces between particles.

### Governing equations for the fluid in CFD

The continuous fluid system is described by a locally averaged Navier–Stokes equation. This has been achieved by discretising the fluid domain into fluid cells by the CFD method, which solves the locally averaged state variables at each cell following the governing equations below (Climent *et al.*, 2014; Li & Zhao, 2018)

$$\begin{cases} \frac{\partial(\varepsilon\rho_f)}{\partial t} + \nabla \cdot (\varepsilon\rho_f U^f) = 0 \\ \frac{\partial(\varepsilon\rho_f)}{\partial t} + \nabla \cdot (\varepsilon\rho_f U^f U^f) - \varepsilon\nabla \cdot (\mu_f \nabla U^f) = -\nabla p - f^p + \varepsilon\rho_f g \end{cases} \quad (8)$$

where  $\varepsilon$  denotes the porosity;  $U^f$  and  $p$  are the average velocity and pressure of a fluid cell, respectively;  $\rho_f$  is the averaged fluid density;  $f^p$  denotes the volumetric interaction force of particles acting on the fluid inside each cell;  $g$  is the acceleration of gravity; and  $\mu_f$  is the fluid viscosity.

### Coupling between the particles and the fluid

The key to the coupling between the CFD and DEM is to properly consider the particle–fluid interaction forces. The interaction forces between fluid and particle are composed of two parts: hydrostatic and hydrodynamic forces. The hydrostatic force acting on a particle is the buoyancy force, while the hydrodynamic force consists of drag force, lift force and virtual mass force (Zhao *et al.*, 2014). In this study, the buoyancy force and drag force are considered as the dominant interaction forces (Zhao & Shan, 2013). The drag force is calculated using the equation proposed by Di Felice (1994), as follows:

$$F^d = \frac{1}{8} C_d \rho_f \pi d_p^2 (U^f - U^p) |U^f - U^p| \varepsilon^{1-\chi} \quad (9)$$

where  $C_d$  is the drag coefficient;  $d_p$  and  $U^p$  are particle diameter and velocity, respectively. The porosity correction function  $\varepsilon^{-\chi}$  captures the effect of packing concentration particles on the drag force. The expression of  $\chi$  is as follows

$$\chi = 3.7 - 0.65 \exp \left[ -\frac{(1.5 - \log_{10} \text{Re}_p)^2}{2} \right] \quad (10)$$

in which the Reynolds number of the particles  $\text{Re}_p$  is expressed by the equation below

$$\text{Re}_p = \frac{\varepsilon \rho_f d_p |U^f - U^p|}{\mu} \quad (11)$$

The buoyant force as a result of the fluid pressure gradient around a single particle is calculated as follows (Kafui *et al.*, 2002; O’Sullivan, 2011)

$$F^b = \frac{1}{6} \pi \rho_f d_p^3 g \quad (12)$$

### Coupling and data exchanging between CFD and DEM

In order to implement the CFD–DEM coupling, DEM and CFD solvers are run consecutively, with data exchanged after a predefined number of time steps of calculation for the two solvers. At each time step, the particles’ positions and velocities are calculated by DEM. This information is then transferred to the CFD and the fluid cells for accommodating the corresponding particles are determined. The locally averaged Navier–Stokes equation is solved by the InterDyMFoam solver to attain the volume fraction and a mean particle velocity for each cell, which can be used to evaluate the momentum exchange terms between the fluid and particle phases. Based on the momentum exchange terms, the fluid flow is calculated and the fluid forces such as drag force and buoyant force acting on the particles are obtained. These interaction forces are then passed to the DEM to calculate the particle system in the subsequent interactive process.

The most important contribution to particle–fluid momentum exchange is the drag force determined by the particle volume fraction. The divide void fraction method is adopted in this study to compute the particle volume fraction. In this method, the actual volume of the particle is considered in a fluid cell, which has been shown to provide more reasonable results than the centre void fraction method (Zhao & Shan, 2013).

### NOTATION

$C_d$	drag force coefficient
$d_p$	diameter of the particle
$E_d$	dissipated energy
$E_i$	initial total energy
$E_k$	kinetic energy
$E_p$	potential energy
$F^b$	buoyant force
$F_i^f$	particle–fluid interaction force acting on particle
$F_i^g$	gravitational force acting on particle
$F_{ij}^c$	contact force acting on particle
$\text{Fr}$	Froude number
$f$	normalised contact force
$f^p$	volumetric interaction force of particles acting on the fluid inside each cell
$g$	acceleration of gravity
$h$	maximum height of the flow
$h_i$	height of any given particle
$h_j$	height of water in any given fluid cell
$I_i$	moment of inertia of a single particle
$M$	total number of fluid cells
$M_{t,ij}$	tangential resistant moment
$M_{r,ij}$	rolling resistant moment
$m_i$	mass of any given particle
$m_j$	mass of water in any given fluid cell

$N$	contact force of each particle
$\langle N \rangle$	average contact force
$p$	pressure of a fluid cell
$R$	total number of particles
$\text{Re}_p$	Reynolds number
$r$	radius of the particle
$U^f$	average velocity of a fluid cell
$U^p$	particle velocity
$U^p_t$	translational velocity of particle
$U_r$	relative settling velocity between the particle and the fluid
$v$	average velocity of the flow front
$v_i$	velocity of any given particle
$v_j$	velocity of water in any given fluid cell
$v_s$	solid fraction
$\omega_i$	angular velocities of particle
$\alpha$	dynamic pressure coefficient
$\varepsilon$	porosity
$\mu_f$	fluid viscosity
$\rho$	flow density
$\rho_f$	density of fluid
$\rho_p$	density of particle
$\Phi$	deviator fabric

### REFERENCES

- Armanini, A., Larcher, M. & Odorizzi, M. (2011). Dynamic impact of a debris flow against a vertical wall. *Ital. J. Engng Geol. Environ.* **11**, 1041–1049.
- Barreto, D. & O’Sullivan, C. (2012). The influence of inter-particle friction and the intermediate stress ratio on soil response under generalised stress conditions. *Granul. Matter* **14**, No. 4, 505–521.
- Chehata, D., Zenit, R. & Wassgren, C. R. (2003). Dense granular flow around an immersed cylinder. *Phys. Fluids* **15**, No. 6, 1622–1631.
- Chiou, M. C., Wang, Y. & Hutter, K. (2005). Influence of obstacles on rapid granular flows. *Acta Mech.* **175**, No. 1–4, 105–122.
- Choi, C. E., Au-Yeung, S. & Ng, C. W. W. (2015a). Flume investigation of landslide granular debris and water runup mechanisms. *Géotechnique Lett.* **5**, No. 1, 28–32.
- Choi, C. E., Ng, C. W. W., Au-Yeung, S. C. H. & Goodwin, G. (2015b). Froude characteristics of both dense granular and water flows in flume modelling. *Landslides* **12**, No. 6, 1197–1206.
- Choi, C. E., Ng, C. W. W., Liu, H. M. & Wang, Y. (2020). Interaction between dry granular flow and rigid barrier with basal clearance: analytical and physical modelling. *Can. Geotech. J.* **57**, No. 2, 236–245, <https://doi.org/10.1139/cgj-2018-0622>.
- Calvetti, F., di Prisco, C. & Vairaktaris, E. (2016). Dry granular flows impacts on rigid obstacles: DEM evaluation of a design formula for the impact force. *Proceedings of 6th Italian conference of researchers in geotechnical engineering*, Bologna, Italy, pp. 290–295.
- Calvetti, F., di Prisco, C. G. & Vairaktaris, E. (2017). DEM assessment of impact forces of dry granular masses on rigid barriers. *Acta Geotech.* **12**, No. 1, 129–144.
- Calvetti, F., Prisco, C. D., Redaelli, I., Sganzerla, A. & Vairaktaris, E. (2019). Mechanical interpretation of dry granular masses impacting on rigid obstacles. *Acta Geotech.* **14**, No. 5, 1289–1305, <https://doi.org/10.1007/s11440-019-00831-9>.
- Climent, N., Arroyo, M., O’Sullivan, C. & Gens, A. (2014). Sand production simulation coupling DEM with CFD. *Eur. J. Environ. Civ. Engng* **18**, No. 9, 983–1008.
- Cui, P., Zeng, C. & Lei, Y. (2015). Experimental analysis on the impact force of viscous debris flow. *Earth Surf. Process. Landf.* **40**, No. 12, 1644–1655.
- Cui, Y., Choi, C. E., Liu, L. H. D. & Ng, C. W. W. (2018). Effects of particle size of mono-disperse granular flows impacting a rigid barrier. *Nat. Hazards* **91**, No. 3, 1179–1201.
- Di Felice, R. (1994). The voidage function for fluid–particle interaction systems. *Int. J. Multiphase Flow* **20**, No. 1, 153–159.
- Gray, J. M. N. T., Tai, Y. C. & Noelle, S. (2003). Shock waves, dead zones and particle-free regions in rapid granular free-surface flows. *J. Fluid Mech.* **491**, 161–181.
- Hákonardóttir, K. M., Hogg, A. J., Johannesson, T., Kren, M. & Tiefenbacher, F. (2003). Large-scale avalanche braking mound

- and catching dam experiments with snow: a study of the airborne jet. *Surv. Geophys.* **24**, No. 5–6, 543–554.
- Hallquist, J. O. (2006). *LS-DYNA theory manual*. Livermore, CA, USA: Livermore Software Technology Corp.
- He, X., Liang, D., Wu, W., Cai, G., Zhao, C. & Wang, S. (2018). Study of the interaction between dry granular flows and rigid barriers with an SPH model. *Int. J. Numer. Analyt. Methods Geomech.* **42**, No. 11, 1217–1234.
- Hong, Y., Wang, L. Z., Zhang, J. F. & Gao, Z. W. (2020). 3D elastoplastic model for fine-grained gassy soil considering the gas-dependent yield surface shape and stress-dilatancy. *J. Engng Mech., ASCE* **146**, No. 5, 04020037, [https://doi.org/10.1061/\(ASCE\)EM.1943-7889.0001760](https://doi.org/10.1061/(ASCE)EM.1943-7889.0001760).
- Hübl, J., Suda, J., Proske, D., Kaitna, R. & Scheidl, C. (2009). Debris flow impact estimation. In *Proceedings of the 11th international symposium on water management and hydraulic engineering (WMHE)* (eds C. Popovska and M. Jovanovski), pp. 137–148. Skopje, Macedonia: Ss Cyril and Methodius University.
- Iverson, R. M. (1997). The physics of debris flows. *Rev. Geophys.* **35**, No. 3, 245–296.
- Iverson, R. M. & George, D. L. (2014). A depth-averaged debris-flow model that includes the effects of evolving dilatancy. I. Physical basis. *Proc. R. Soc. London A: Math., Phys. Engng Sci.* **470**, No. 2170, article 20130819.
- Jóhannesson, T., Gauer, P., Issler, D. & Lied, K. (2009). *The design of avalanche protection dams: recent practical and theoretical developments*. Brussels, Belgium: European Commission.
- Kafui, K. D., Thornton, C. & Adams, M. J. (2002). Discrete particle–continuum fluid modelling of gas–solid fluidised beds. *Chem. Engng Sci.* **57**, No. 13, 2395–2410.
- Kawano, K., Shire, T. & O’Sullivan, C. (2017). Coupled DEM–CFD analysis of the initiation of internal instability in a gap-graded granular embankment filter. *EPJ Web of Conferences* **140**, 10005.
- Koo, R. C. H., Kwan, J. S. H., Lam, C., Ng, C. W. W., Yiu, J., Choi, C. E., Ng, A. K. L., Ho, K. K. S. & Pun, W. K. (2016). Dynamic response of flexible rockfall barriers under different loading geometries. *Landslides* **14**, No. 3, 905–916.
- Kwan, J. S. H. (2012). *Supplementary technical guidance on design of rigid debris-resisting barriers*, Technical Note No. TN 2/2012. Hong Kong, China: Geotechnical Engineering Office, Civil Engineering and Development Department, The HKSAR Government.
- Kwan, J. H. S., Koo, R. C. H. & Ng, C. W. W. (2015). Landslide mobility analysis for design of multiple debris-resisting barriers. *Can. Geotech. J.* **52**, No. 9, 1345–1359.
- Li, X. & Zhao, J. (2018). Dam-break of mixtures consisting of non-Newtonian liquids and granular particles. *Powder Technol.* **338**, 493–505.
- McArdell, B. W., Bartelt, P. & Kowalski, J. (2007). Field observations of basal forces and fluid pore pressure in a debris flow. *Geophys. Res. Lett.* **34**, No. 7, L07406.
- Ng, C. W. W., Song, D., Choi, C. E., Koo, R. C. H. & Kwan, J. S. H. (2016). A novel flexible barrier for landslide impact in centrifuge. *Geotechnique Lett.* **6**, No. 3, 221–225, <https://doi.org/10.1680/jgele.16.00048>.
- Ng, C. W. W., Song, D., Choi, C. E., Liu, L. H. D., Kwan, J. S. H., Koo, R. C. H. & Pun, W. K. (2017a). Impact mechanisms of granular and viscous flows on rigid and flexible barriers. *Can. Geotech. J.* **54**, No. 2, 188–206.
- Ng, C. W. W., Choi, C. E., Liu, L. H. D. & Yang, N. (2017b). Influence of particle size on the mechanisms of dry granular runup on a rigid barrier. *Geotechnique Lett.* **7**, No. 1, 79–89, <https://doi.org/10.1680/jgele.16.00159>.
- Ng, C. W. W., Choi, C. E., Koo, R. C. H., Goodwin, G. R., Song, D. & Kwan, J. S. H. (2018). Dry granular flow interaction with dual-barrier systems. *Geotechnique* **68**, No. 5, 386–399, <https://doi.org/10.1680/jgeot.16.P.273>.
- O’Sullivan, C. (2011). *Particulate discrete element modelling: a geomechanics perspective*. London, UK: Spon Press.
- O’Sullivan, C., Wadee, M. A., Hanley, K. J. & Barreto, D. (2013). Use of DEM and elastic stability analysis to explain the influence of the intermediate principal stress on shear strength. *Geotechnique* **63**, No. 15, 1298–1309, <https://doi.org/10.1680/geot.12.P.153>.
- Peng, C., Guo, X., Wu, W. & Wang, Y. (2016). Unified modelling of granular media with smoothed particle hydrodynamics. *Acta Geotech.* **11**, No. 6, 1231–1247.
- Pierson, T. C. (2005). Hyperconcentrated flow-transitional process between water flow and debris flow. In *Debris-flow hazards and related phenomena* (eds M. Jakob and O. Hungr), pp. 159–202. Berlin/Heidelberg, Germany: Springer.
- Pudasaini, S. P. & Hutter, K. (2007). *Avalanche dynamics*. Berlin, Germany: Springer.
- Scheidl, C., Chiari, M., Kaitna, R., Müllegger, M., Krawtschuk, A., Zimmermann, T. & Proske, D. (2013). Analysing debris-flow impact models, based on a small scale modelling approach. *Surv. Geophys.* **34**, No. 1, 121–140.
- Shan, T. & Zhao, J. D. (2014). A coupled CFD–DEM analysis of granular flow impacting on water reservoir. *Acta Mech.* **225**, No. 8, 2449–2470.
- Shire, T. & O’Sullivan, C. (2013). Micromechanical assessment of an internal stability criterion. *Acta Geotech.* **8**, No. 1, 81–90.
- Song, D., Ng, C. W. W., Choi, C. E., Kwan, J. S. H. & Koo, R. C. H. (2017). Influence of debris flow solid fraction on rigid barrier impact. *Can. Geotech. J.* **54**, No. 10, 1421–1434.
- Stokes, G. G. (1844). On the theories of internal friction of fluids in motion and of the equilibrium and motion of elastic solids. *Trans. Cambridge Phil. Soc.* **8**, No. 9, 287–319.
- Su, T. C., O’Sullivan, C., Nagira, T., Yasuda, H. & Gourlay, C. M. (2018). Semi-solid deformation of Al–Cu alloys: a quantitative comparison between real-time imaging and coupled LBM–DEM simulations. *Acta Mater.* **163**, 208–225, <https://doi.org/10.1016/j.actamat.2018.10.006>.
- Teufelsbauer, H., Wang, Y., Pudasaini, S. P., Borja, R. I. & Wu, W. (2011). DEM simulation of impact force exerted by granular flow on rigid structures. *Acta Geotech.* **6**, No. 3, 119–133.
- Thornton, C. (2000). Numerical simulations of deviator shear deformations of granular media. *Geotechnique* **50**, No. 1, 43–53, <https://doi.org/10.1680/geot.2000.50.1.43>.
- Utili, S., Zhao, T. & Houlsby, G. T. (2015). 3D DEM investigation of granular column collapse: evaluation of debris motion and its destructive power. *Engng Geol.* **186**, 3–16.
- Wendeler, C., McArdell, B. W., Rickenmann, D., Volkwein, A., Roth, A. & Denk, M. (2006). Field testing and numerical modelling of flexible debris flow barriers. In *Physical modelling in geotechnics* (eds C. W. N. Ng, Y. H. Wang and L. M. Zhang), vol. 2, pp. 1573–1578. Boca Raton, FL, USA: CRC Press.
- Yimsiri, S. & Soga, K. (2010). DEM analysis of soil fabric effects on behaviour of sand. *Geotechnique* **60**, No. 6, 483–495, <https://doi.org/10.1680/geot.2010.60.6.483>.
- Zakeri, A., Hoeg, K. & Nadim, F. (2009). Submarine debris flow impact on pipelines: numerical modeling of drag forces for mitigation and control measures. *SPE Projects, Facilities Constr.* **4**, No. 1, 1–11.
- Zhao, J. & Shan, T. (2013). Coupled CFD–DEM simulation of fluid–particle interaction in geomechanics. *Powder Technol.* **239**, No. 17, 248–258.
- Zhao, T., Houlsby, G. T. & Utili, S. (2014). Investigation of granular batch sedimentation via DEM–CFD coupling. *Granul. Matter* **16**, No. 6, 921–932.
- Zheng, H. C., Shi, Z. M., Peng, M. & Yu, S. B. (2018). Coupled CFD–DEM model for the direct numerical simulation of sediment bed erosion by viscous shear flow. *Engng Geol.* **245**, 309–321.
- Zhou, W., Lai, Z., Ma, G., Yang, L. & Chen, Y. (2016). Effect of base roughness on size segregation in dry granular flows. *Granul. Matter* **18**, No. 4, article 83, <https://doi.org/10.1007/s10035-016-0680-7>.